

# Metallicity dependence of dust growth in a protoplanetary disk

Ryoki Matsukoba<sup>1,2</sup>, Eduard I. Vorobyov<sup>3,4</sup>, and Takashi Hosokawa<sup>1</sup>

<sup>1</sup> Department of Physics, Graduate School of Science, Kyoto University, Sakyo, Kyoto 606-8502, Japan  
e-mail: r.matsukoba@tap.scphys.kyoto-u.ac.jp

<sup>2</sup> Center for Computational Sciences, University of Tsukuba, Ten-nodai, 1-1-1 Tsukuba, Ibaraki 305-8577, Japan

<sup>3</sup> Department of Astrophysics, University of Vienna, Türkenschanzstrasse 17, 1180, Vienna, Austria

<sup>4</sup> Research Institute of Physics, Southern Federal University, Roston-on-Don 344090, Russia

## ABSTRACT

**Aims.** In the context of planet formation, growth from micron-sized grains to kilometer-sized planetesimals is a crucial question. Since the dust growth rate depends on the amount of dust, realizing planet formation scenarios based on dust growth is challenging in environments with low metallicity, i.e. less dust. We investigate dust growth during disk evolution, particularly focusing on the relationship with metallicity.

**Methods.** We perform two-dimensional thin-disk hydrodynamic simulations to track the disk evolution over 300 kyr from its formation. The dust motion is solved separately from the gas motion, with its distribution changing due to drag forces from the gas. Dust size growth is also accounted for, with the magnitude of the drag force varying according to the dust size. We employ three models with metallicities of 1.0, 0.1, and 0.01  $Z_{\odot}$ , i.e. dust-to-gas mass ratios of  $10^{-2}$ ,  $10^{-3}$ , and  $10^{-4}$ , respectively.

**Results.** In the disks with the metallicities  $\geq 0.1 Z_{\odot}$ , the dust radii reach cm sizes, consistent with estimations from the dust growth timescale. Conversely, for the metallicity of 0.01  $Z_{\odot}$ , the maximum dust size is only  $10^{-2}$  cm, with almost no growth observed across the entire disk scale ( $\sim 100$  au). At the metallicities  $\geq 0.1 Z_{\odot}$ , the decoupling between grown dust and gas leads to non-uniform dust-to-gas mass ratios. However, deviations from the canonical value of this ratio have no impact on the gravitational instability of the disk. The formation of dust rings is confirmed in the innermost part of the disk ( $\sim 10$ – $30$  au). The dust rings where the dust-to-gas mass ratio is enhanced, and the Stokes number reaches  $\sim 0.1$ , are suitable environments for the streaming instability. We conjecture that planetesimal formation occurs through the streaming instability in these dust rings.

**Key words.** Protoplanetary disks – Stars: formation – Planets and satellites: formation – methods: numerical – Hydrodynamics

## 1. Introduction

Recent observations of exoplanets have highlighted the ubiquity of planetary systems in the present-day Universe, revealing that a multitude of stars host their own planets (NASA Exoplanet Archive; Akeson et al. 2013). Although the foundational mechanisms of planet formation remain shrouded in mystery, efforts to unravel them are progressively advancing (see Drążkowska et al. 2023, for a review).

One of the main challenges in planet formation is understanding the growth process from micron-sized grains, prevalent in early protoplanetary disks, to kilometer-sized planetesimals, the building blocks of planets. Dust grains within a protoplanetary disk rotate at Keplerian velocities. Meanwhile, gas is supported by gas pressure and rotates at sub-Keplerian velocities. As a result, dust grains experience a headwind, lose angular momentum, and drift radially toward the central star. In the minimum mass solar nebula (MMSN; Hayashi 1981), when the size of dust grains is in the range of a centimeter to a meter, the drift velocity reaches its maximum, causing the dust to fall into the central star before it can grow further. This phenomenon is known as the “radial drift barrier” (Whipple 1972; Adachi et al. 1976; Weidenschilling 1977). Therefore, suppressing dust drift is essential for the formation of planetesimals.

One of the most classical pictures for planetesimal formation is the gravitational instability of a dust layer accumulated in the midplane of the protoplanetary disk (Safronov 1972; Goldreich & Ward 1973). However, achieving such a dense dust

layer is deemed difficult because turbulence generated by vertical shear stirs up the dust layer (Weidenschilling 1980). Instead, some mechanisms have been proposed to induce dust concentration, such as dust-driven instabilities (Ward 1976; Takahashi & Inutsuka 2014; Tominaga et al. 2019, 2021) and dust trapping by substructures in the disk (Haghighipour & Boss 2003; Johansen et al. 2009; Nayakshin 2017b; Vorobyov & Elbakyan 2019). The pathway to planetesimal formation through streaming instability is actively investigated by many previous studies (e.g., Youdin & Goodman 2005; Johansen & Youdin 2007; Youdin & Johansen 2007; Yang et al. 2017; Carrera & Simon 2022). The streaming instability, a type of dust-driven instability, arises from the relative drift between dust and gas. This mechanism requires dust sizes in the millimeter to centimeter range in order to moderate coupling with gas. If the streaming instability grows and evolves in a non-linear regime, it leads to strong dust clumping. Subsequently, dust-dense regions collapse into planetesimals due to dust self-gravity once the local dust density exceeds the Roche density (e.g., Johansen et al. 2007; Simon et al. 2016).

In the dust-driven instabilities, it is preferred for the dust grains to be of mm to cm in size, as this size range allows them to moderately decouple from the gas motion by aerodynamic drag. For this reason, the distribution of dust size is crucial for considering these instabilities. Furthermore, high dust-to-gas mass ratios, typically greater than that of solar metallicity (0.01), are required to promote instability. Dust size growth depends on the amount of dust in the disk, with greater amounts of dust leading to faster growth rates. Therefore, disks with high initial dust-to-

gas mass ratios, indicative of high metallicity, are advantageous for the realization of these instabilities.

The occurrence rate of planets is correlated with the metallicity of their host stars; however, this correlation varies according to the type of planet. The occurrence rates for gas giants and sub-Neptune planets exhibit a positive correlation with the metallicity of their host stars (Santos et al. 2004; Petigura et al. 2018). In contrast, the correlation for super-Earth planets shows a weak dependence on metallicity (Wang & Fischer 2015), or it may even be absent (Mulders et al. 2016; Kutra et al. 2021). These variations in metallicity dependence arise from differences in the formation mechanisms of each type of planet and are likely influenced by the environments in which their precursors, the planetesimals, form.

In this study, we use two-dimensional numerical simulations to consistently track the growth of dust grains during the formation and evolution of the protoplanetary disk. We investigate the impact of the amount of dust on the efficiency of dust grain growth and its effect on the spatial distribution of dust grains, using three models with different metallicities (dust-to-gas mass ratios). Our calculations monitor the disk evolution and dust growth over a period of 300 kyr following the formation of the disk. This long-term simulation is unprecedented and provides valuable insights into dust growth within a disk of low metallicity, where dust growth is slow.

This paper is organized as follows: We describe our simulation method and setup in Section 2. We present the simulation results and explain the disk evolution and dust growth for each model in Section 3. We then discuss the potential for planetesimal and planet formation within the disk in Section 4. Summary is given in Section 5.

## 2. Method

We simulate dust growth in protoplanetary disks with different metallicities using the Formation and Evolution of Stars and Disks (FEOSAD) code presented in Vorobyov et al. (2018) and modified to include the backreaction of dust on gas in Vorobyov et al. (2020b). FEOSAD solves the equations of hydrodynamics in the thin-disk limit for a gas-dust system. The numerical simulations start from the gravitational collapse of a flattened pre-stellar cloud and the protoplanetary disk is formed self-consistently as a result of angular momentum conservation of the contracting cloud. In this work, for the first time, we applied FEOSAD to non-solar metallicity environments and the usual energy balance equation was modified to include thermal processes that may be important at low metallicity as described in Vorobyov et al. (2020c).

The integration of hydrodynamics equations in the polar coordinates  $(r, \phi)$  was carried out using a finite-volume method with a time-explicit solution procedure similar in methodology to the ZEUS code (Stone & Norman 1992). The advection of gas and dust is treated using the third-order-accurate piecewise-parabolic interpolation scheme of Colella & Woodward (1984). The stellar mass grows according to the mass accretion rate through the inner computational boundary and the properties of the protostar are calculated using the stellar evolution tracks obtained with the STELLAR code for the respective metallicity (Yorke & Bodenheimer 2008; Hosokawa & Omukai 2009).

In this work, we are focused on gas and dust dynamics at the intermediate and outer disk regions. Therefore, the central 10 au were cut out and replaced with a sink cell, while the entire computational domain extends to several thousands of astronomical units. The numerical grid contains  $1028 \times 1028$  cells, which are

logarithmically spaced in the radial direction and linearly in the azimuthal one, providing sub-au resolution up to a distance of  $\approx 150$  au. Below, we provide the basic equations and initial conditions. More details can be found in the aforementioned articles.

### 2.1. Basic equations for the gaseous component

The system of equations for the gaseous component consists of the continuity equation, equations describing the gas dynamics, and the energy balance equation. The dynamics of gas is governed by the stellar and disk gravity, turbulent viscosity, and friction between gas and dust. The pertinent equations in the thin-disk limit are as follows.

$$\frac{\partial \Sigma_g}{\partial t} + \nabla_p \cdot (\Sigma_g \mathbf{v}_p) = 0, \quad (1)$$

$$\frac{\partial}{\partial t} (\Sigma_g \mathbf{v}_p) + \left[ \nabla \cdot (\Sigma_g \mathbf{v}_p \otimes \mathbf{v}_p) \right]_p = -\nabla_p \mathcal{P} + \Sigma_g \mathbf{g}_p + (\nabla \cdot \mathbf{\Pi})_p - \Sigma_{d,gr} \mathbf{f}_p, \quad (2)$$

where the planar components  $(r, \phi)$  are denoted by the subscript  $p$ ,  $\Sigma_g$  is the gas surface density,  $\mathbf{v}_p = v_r \hat{\mathbf{r}} + v_\phi \hat{\boldsymbol{\phi}}$  is the gas velocity in the disk plane,  $\mathcal{P}$  is the pressure, integrated in the vertical direction using the ideal equation of state  $\mathcal{P} = (\gamma - 1)e$  with the internal energy  $e$ , and  $\mathbf{f}_p$  is the drag force per unit mass between gas and dust. The gravitational acceleration in the disk plane  $\mathbf{g}_p$  takes into account gas and dust self-gravity in the disk and the gravity of the central star when it is formed. The gas and dust disk self-gravity is calculated using the convolution method described in detail in Binney & Tremaine (1987). To compute the viscous stress tensor  $\mathbf{\Pi}$ , we parameterise the kinematic viscosity using the usual  $\alpha$ -parameter approach with the value of  $\alpha$  set equal to  $10^{-4}$  throughout the disk.

The internal energy balance equation is written as

$$\frac{\partial e}{\partial t} + \nabla_p \cdot (e \mathbf{v}_p) = -\mathcal{P} (\nabla_p \cdot \mathbf{v}_p) - \Lambda + (\nabla v)_{pp'} : \Pi_{pp'}, \quad (3)$$

where  $\Lambda$  encompasses the cooling/heating processes that are pertinent to protoplanetary disks at solar and lower metallicities. In particular, we considered the following processes: the continuum emissions of gas and dust, molecular line emissions of  $\text{H}_2$  and HD, fine-structure line emissions of O I ( $63 \mu\text{m}$ ) and C II ( $158 \mu\text{m}$ ), and chemical cooling/heating associated with H ionization/recombination and  $\text{H}_2$  dissociation/formation. In addition, we solved the non-equilibrium chemical network for eight species, H,  $\text{H}_2$ ,  $\text{H}^+$ ,  $\text{H}^-$ , D, HD,  $\text{D}^+$ , and  $\text{e}^-$ , with 27 reactions. The evolution of the chemical components affects the cooling rates due to molecular line emissions and chemical cooling. The dust temperature is calculated from the energy balance on dust grains due to the thermal emission, absorption, and collision with gas. This approach permits decoupling of the gas and dust temperatures in the low-density or high-temperature regime or at low metallicity. More details on the thermal scheme applied in this work can be found in Vorobyov et al. (2020c).

### 2.2. Basic equations for the dust component

The dust component in our model is divided into two populations: (i) small dust, which are grains with a size<sup>1</sup> between  $a_{\min} = 5 \times 10^{-3} \mu\text{m}$  and  $a_* = 1 \mu\text{m}$  and (ii) grown dust ranging in size from  $a_*$  to a maximum value  $a_{\max}$ , which is variable

<sup>1</sup> By the size of dust grains we understand its radius.

in space and time. Initially, all dust in a collapsing pre-stellar cloud is in the form of small dust grains. Small dust can grow and turn into grown dust as the disk forms and evolves. Dust in both populations is distributed over size according to a simple power law:

$$N(a) = C \cdot a^{-q}, \quad (4)$$

where  $N(a)$  is the number of dust particles per unit dust size,  $C$  is a normalization constant, and  $q = 3.5$ . We note that the power index  $q$  is kept constant during the considered disk evolution period for simplicity.

We solve the continuity equations separately for the grown and small dust ensembles. However, the momentum equation is solved only for the grown dust, because small dust is assumed to be dynamically linked to the gas. The system of hydrodynamic equations for the two-population dust ensemble in the zero-pressure limit is written as:

$$\frac{\partial \Sigma_{\text{d,sm}}}{\partial t} + \nabla_{\text{p}} \cdot (\Sigma_{\text{d,sm}} \mathbf{v}_{\text{p}}) = -S(a_{\text{max}}), \quad (5)$$

$$\frac{\partial \Sigma_{\text{d,gr}}}{\partial t} + \nabla_{\text{p}} \cdot (\Sigma_{\text{d,gr}} \mathbf{u}_{\text{p}}) = S(a_{\text{max}}), \quad (6)$$

$$\begin{aligned} \frac{\partial}{\partial t} (\Sigma_{\text{d,gr}} \mathbf{u}_{\text{p}}) + \left[ \nabla \cdot (\Sigma_{\text{d,gr}} \mathbf{u}_{\text{p}} \otimes \mathbf{u}_{\text{p}}) \right]_{\text{p}} &= \Sigma_{\text{d,gr}} \mathbf{g}_{\text{p}} + \\ &+ \Sigma_{\text{d,gr}} \mathbf{f}_{\text{p}} + S(a_{\text{max}}) \mathbf{v}_{\text{p}}, \end{aligned} \quad (7)$$

where  $\Sigma_{\text{d,sm}}$  and  $\Sigma_{\text{d,gr}}$  are the surface densities of small and grown dust, respectively, and  $\mathbf{u}_{\text{p}}$  are the planar components of the grown dust velocity.

The grown dust dynamics is sensitive to the properties of surrounding gas. The drag force (per unit mass) links dust with gas and can be written according to Weidenschilling (1977) as:

$$\mathbf{f}_{\text{p}} = \frac{1}{2m_{\text{d}}} C_{\text{D}} \sigma \rho_{\text{g}} (\mathbf{v}_{\text{p}} - \mathbf{u}_{\text{p}}) |\mathbf{v}_{\text{p}} - \mathbf{u}_{\text{p}}|, \quad (8)$$

where  $\sigma$  is the dust grain cross section,  $\rho_{\text{g}}$  the volume density of gas,  $m_{\text{d}}$  the mass of a dust grain, and  $C_{\text{D}}$  the dimensionless friction parameter. The functional expression for the latter is taken from Henderson (1976) and is described in detail in Vorobyov et al. (2023). The use of the Henderson friction coefficient allows us to treat the drag force avoiding discontinuities in two different regimes: the Epstein regime, and Stokes linear and non-linear regimes. The advantages of the Henderson friction coefficient over the more common drag coefficient proposed by Weidenschilling (1977) are discussed in Stoyanovskaya et al. (2020). To account for the back-reaction of grown dust on dust, the term  $\Sigma_{\text{d,gr}} \mathbf{f}_{\text{p}}$  is symmetrically included in both the gas and dust momentum equations. We use the maximum size of dust grains  $a_{\text{max}}$  when calculating the value of  $m_{\text{d}}$  in Equation (8). The friction force  $\mathbf{f}_{\text{p}}$  thus derived would describe the dynamics of the main dust mass carriers, since large grains near  $a_{\text{max}}$  mostly determine the value of  $m_{\text{d}}$  for the chosen value of  $q = 3.5$ .

The term  $S(a_{\text{max}})$  that enters the equations for the dust component is the conversion rate between small and grown dust populations. We assumed that the distribution of dust particles over size follows the form given by Equation (4) for both small and grown populations. Furthermore, the distribution is assumed to be continuous at  $a_*$ . Our scheme is constructed so as to preserve continuity at  $a_*$  by writing the conversion rate of small to grown dust in the following form:

$$S(a_{\text{max}}) = -\frac{\Delta \Sigma_{\text{d,sm}}}{\Delta t}, \quad (9)$$

where

$$\Delta \Sigma_{\text{d,sm}} = \Sigma_{\text{d,sm}}^{n+1} - \Sigma_{\text{d,sm}}^n = \frac{\Sigma_{\text{d,gr}}^n \int_{a_{\text{min}}}^{a_*} a^{3-q} da - \Sigma_{\text{d,sm}}^n \int_{a_*}^{a_{\text{max}}^{n+1}} a^{3-q} da}{\int_{a_{\text{min}}}^{a_{\text{max}}^{n+1}} a^{3-q} da}, \quad (10)$$

where indices  $n$  and  $n + 1$  denote the current and next hydrodynamic steps of integration, respectively, and  $\Delta t$  is the hydrodynamic time step. The adopted scheme effectively assumes that dust growth smooths out any discontinuity in the dust size distribution at  $a_*$  that may appear due to differential drift of small and grown dust populations. A more detailed description of the scheme is presented in Molyarova et al. (2021) and Vorobyov et al. (2022).

The conversion rate  $S(a_{\text{max}})$  depends only on the local maximal size of dust  $a_{\text{max}}$ , since the values of  $a_{\text{min}}$  and  $a_*$  are fixed in our model. At the beginning of the cloud core collapse, all grains are in the form of small dust, namely,  $a_{\text{max}} = 1.0 \mu\text{m}$ . During the disk formation and evolution epoch the maximal size of dust particles usually increases. The change in  $a_{\text{max}}$  within a particular numerical cell in our model occurs due to collisional growth or via advection of dust through the cell. The equation describing the dynamical evolution of  $a_{\text{max}}$  is as follows:

$$\frac{\partial a_{\text{max}}}{\partial t} + (\mathbf{u}_{\text{p}} \cdot \nabla_{\text{p}}) a_{\text{max}} = \mathcal{D}, \quad (11)$$

where the rate of dust growth due to collisions and coagulation is computed in the monodisperse approximation (Birnstiel et al. 2012)

$$\mathcal{D} = \frac{\rho_{\text{d}} u_{\text{rel}}}{\rho_{\text{s}}}. \quad (12)$$

This rate includes the total volume density of dust  $\rho_{\text{d}}$ , the dust material density  $\rho_{\text{s}} = 3.0 \text{ g cm}^{-3}$ , and the relative velocity of particle-to-particle collisions defined as  $u_{\text{rel}} = (u_{\text{th}}^2 + u_{\text{turb}}^2)^{1/2}$ , where  $u_{\text{th}}$  and  $u_{\text{turb}}$  account for the Brownian and turbulence-induced local motion, respectively. When calculating the volume density of dust, we take into account dust settling by calculating the effective scale height of grown dust  $H_{\text{d}}$  via the corresponding gas scale height  $H_{\text{g}}$ ,  $\alpha$  parameter, and the Stokes number as

$$H_{\text{d}} = H_{\text{g}} \sqrt{\frac{\alpha}{\alpha + \text{St}}}. \quad (13)$$

The Stokes number is defined as:

$$\text{St} = \frac{\Omega_{\text{K}} \rho_{\text{s}} a_{\text{max}}}{\rho_{\text{g}} c_{\text{s}}}, \quad (14)$$

where  $\Omega_{\text{K}} = \sqrt{GM_*/r^3}$  represents the Keplerian angular velocity with the central stellar mass  $M_*$ ,  $\rho_{\text{g}}$  is the volume density of gas, and  $c_{\text{s}}$  is the sound speed.

Dust growth in our model is limited by collisional fragmentation and drift. We note that the drift barrier is accounted for self-consistently via the computation of the grown dust dynamics. The fragmentation barrier is taken into account by calculating the characteristic fragmentation size as (Birnstiel et al. 2016):

$$a_{\text{frag}} = \frac{2 \Sigma_{\text{g}} u_{\text{frag}}^2}{3 \pi \rho_{\text{s}} \alpha c_{\text{s}}^2}, \quad (15)$$

where  $u_{\text{frag}}$  is the fragmentation velocity, namely, a threshold value of the relative velocity of dust particles at which collisions result in fragmentation rather than coagulation. In the current study, we adopt  $u_{\text{frag}} = 3 \text{ m s}^{-1}$  (Blum 2018). If  $a_{\text{max}}$  becomes greater than  $a_{\text{frag}}$ , we halt the growth of dust and set  $a_{\text{max}} = a_{\text{frag}}$ .

**Table 1.** The initial parameters of the pre-stellar cloud cores

Metallicity $Z_{\odot}$	Dust-to-gas mass ratio	$\Sigma_0$ g cm <sup>-2</sup>	$c_{s,0}$ km s <sup>-1</sup>	$T_0$ K	$\rho_0$ g cm <sup>-3</sup>	$r_0$ au	$\Omega_0$ km s <sup>-1</sup> pc <sup>-1</sup>	$M_{\text{cloud}}$ $M_{\odot}$
1.0	10 <sup>-2</sup>	9.0 × 10 <sup>-2</sup>	0.19	10	3.8 × 10 <sup>-18</sup>	1600	2.1	0.88
0.1	10 <sup>-3</sup>	9.8 × 10 <sup>-2</sup>	0.21	12	3.8 × 10 <sup>-18</sup>	1700	2.1	0.88
0.01	10 <sup>-4</sup>	0.70	0.33	31	7.6 × 10 <sup>-17</sup>	620	9.4	0.89

**Notes.**  $\Sigma_0$  is the surface density at the plateau,  $c_{s,0}$  is the initial sound speed,  $T_0$  is the initial temperature,  $\rho_0$  is the initial mass density,  $r_0$  is the plateau radius,  $\Omega_0$  is the angular velocity at the plateau, and  $M_{\text{cloud}}$  is the cloud mass.

### 2.3. Initial conditions

The initial gas surface density and angular velocity profiles of the cloud core we set are derived from an axisymmetric cloud collapse where the angular momentum remains constant (Basu 1997):

$$\Sigma_{\text{g}} = \frac{\Sigma_0}{\sqrt{1 + (r/r_0)^2}}, \quad (16)$$

$$\Omega = 2\Omega_0 \left(\frac{r_0}{r}\right)^2 \left[ \sqrt{1 + \left(\frac{r}{r_0}\right)^2} - 1 \right]. \quad (17)$$

The above profile has a plateau with a uniform surface density extending to the radius  $r_0$ ,  $\Sigma_0$  and  $\Omega_0$  are the surface density and angular velocity at the plateau, respectively. The plateau radius  $r_0$  is proportional to the Jeans length

$$r_0 = A \frac{c_{s,0}}{\sqrt{\pi G \rho_0}}, \quad (18)$$

where  $A$  is a constant parameter,  $c_{s,0}$  is the initial sound speed,  $G$  is the gravitational constant, and  $\rho_0$  is the initial mass density. The initial mass and the plateau surface densities are related as  $\Sigma_0 = r_0 \rho_0$ . The constant  $A$  is a parameter defining the initial density perturbation. We set  $A = \sqrt{1.2}$ , with which the ratio of the cloud thermal and gravitational energies is 0.8. We also set the ratio of the rotational and gravitational energies as  $7 \times 10^{-3}$  by adjusting the plateau angular velocity  $\Omega_0$ .

We calculate three models with different metallicities, i.e., different dust-to-gas mass ratios. These models have metallicities of 1.0, 0.1, and 0.01  $Z_{\odot}$ , with corresponding dust-to-gas mass ratios of 10<sup>-2</sup>, 10<sup>-3</sup>, and 10<sup>-4</sup>, respectively. The initial dust-to-gas mass ratio in the gravitationally contracting cloud is spatially uniform.

To constrain the free parameters of the initial surface density configuration, namely,  $c_{s,0}$  and  $\rho_0$ , we make use of a one-zone model developed by Omukai et al. (2005), which derives the relationship between the central density and temperature in clouds of different metallicity. We note that the gas temperature varies with metallicity and models with different metallicities are characterized by distinct initial sound speeds  $c_{s,0}$ . To simulate the evolution of the disk formed from a cloud of nearly solar mass, we select densities and temperatures at which the Jeans mass approximates solar mass, based on the derived density-temperature relationship of Omukai et al. (2005). These selections help determine the initial mass density  $\rho_0$  and the initial sound speed  $c_{s,0}$ . The plateau radius is then calculated from Equation (18) using these initial conditions, and the initial gas surface density  $\Sigma_0$  is determined as  $\Sigma_0 = r_0 \rho_0$ . Table 1 summarizes the values for the initial pre-stellar cloud conditions in each model. Regarding the dust surface density, we assume that it consists solely of small

dust grains, and its density is scaled from the gas surface density in accordance with the dust-to-gas mass ratio.

The initial density is perturbed with an amplitude  $A$ , leading to gravitational collapse of the pre-stellar cloud. The cloud contracts, while simultaneously spinning up. The protoplanetary disk forms when the in-spiraling material of the contracting cloud hits the centrifugal barrier near the inner computational boundary. This occurs when the centrifugal radius of the infalling gas exceeds the sink cell radius of 10 au after about twice the free-fall time elapsed from the onset of cloud collapse. Subsequently, the disk gains matter from the infalling parental cloud while losing it via accretion onto a star introduced within the sink cell. We follow the evolution of the disk and the growth of dust for 300 kyr after the disk formation.

## 3. Global disk evolution and dust growth

Here, we describe the global evolution of a protoplanetary disk and dust growth within the disk at three different metallicities. We present our simulation results for the cases of solar metallicity and low metallicities in Sections 3.1 and 3.2, respectively. Since the results for the solar metallicity case are similar to those of previous studies (e.g., Vorobyov & Elbakyan 2018, 2019), we provide only a brief overview of the solar metallicity case.

### 3.1. Solar metallicity

Figure 1 shows the evolution of the disk from its formation to the last period at 300 kyr. The panels in the left column display the spatial distributions of gas surface density, indicating that the disk's size expands over time. The white contour lines in the panels show isosurface density lines of 0.1 g cm<sup>-2</sup>, serving as a rough indicator of the outer edge of the disk. We note that at 20 kyr (panel i-a), the density at the outer edge exceeds 0.1 g cm<sup>-2</sup>, leading to a disparity between the outer edge and the contour line. The disk extends to approximately 200–300 au at 50 kyr, and around 600 au at 300 kyr.

Panels i-b, i-c, and i-d show that, at 50, 130, and 300 kyr, non-axisymmetric structures like spiral arms appear within the disk, and several clumps exist. This suggests that the disk is gravitationally unstable. In particular, disk fragmentation is most intense around 100 kyr (panel i-c). Thereafter, it gradually calms down, and only one clump remains within the disk at 300 kyr (panel i-d).

In panels i-b and i-c, there are zonal regions with densities exceeding 0.1 g cm<sup>-2</sup>, which extend beyond the panel boundaries. These regions represent remnants of clumps ejected from the central part. Multiple ejection events are observed between 30 and 210 kyr in this run. These events, triggered by gravitational interactions and close encounters between clumps, occur more frequently during periods of intense fragmentation. Ejected clumps escape from the stellar system and may serve as a source

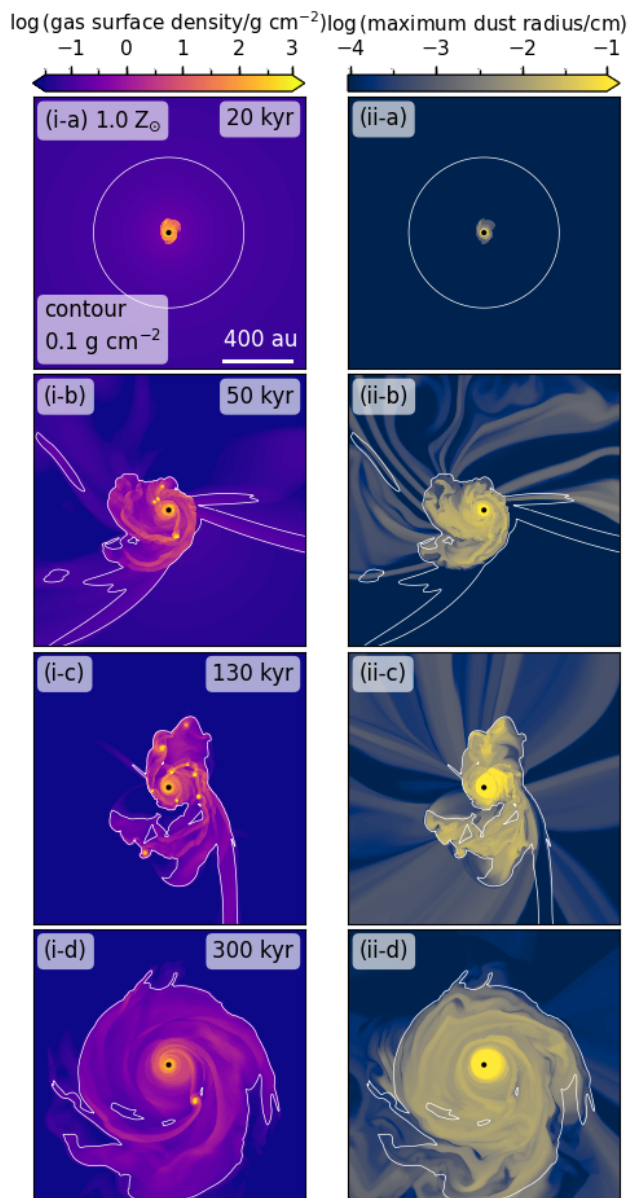


**Fig. 1.** Time evolution of the disk in the case of  $1.0 Z_{\odot}$ . The left and right columns show the 2D distributions of the gas surface density and the maximum dust size at four different epochs, 20, 50, 130, and 300 kyr after the formation of the disk. In each panel, the white contour line delineates an isosurface density of  $0.1 \text{ g cm}^{-2}$ , indicating the approximate location of the outer edge of the disk.

for freely floating brown dwarfs and even planetary-mass objects (Bate 2009; Stamatellos & Whitworth 2009; Basu & Vorobyov 2012; Vorobyov 2016).

The panels in the right column of Figure 1 display the spatial distributions of the maximum dust size. At 20 kyr (panel ii-a), dust growth is observed within a region inside  $\sim 100$  au, corresponding to the disk radius. Subsequently, as the disk radius expands, the area containing large dust grains ( $> 10^{-3}$  cm) also increases. At 300 kyr (panel ii-d), the regions with the large dust grains mainly lie inside the white isodensity lines, indicating that dust growth occurs within the disk. Panels ii-b and ii-c indicate

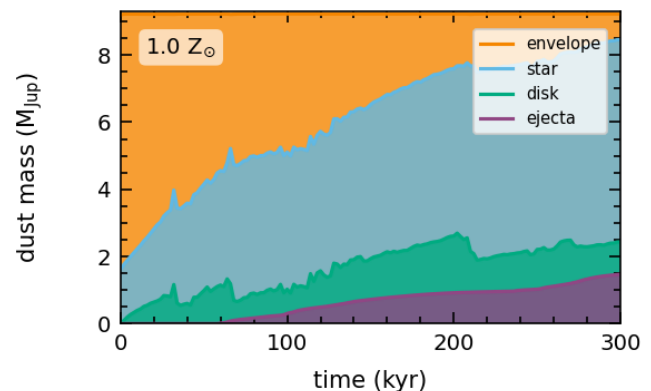


**Fig. 2.** Stacked area chart for the dust mass in the case of  $1.0 Z_{\odot}$ . The dust mass is the sum of the masses of grown and small dust grains. The colors represent four different components: the envelope (orange), central star (blue), disk (green), and ejecta (purple).

the ejection events, characterized by dust grains ranging from  $10^{-3}$  to  $10^{-2}$  cm in size, dispersing radially from the outer edge of the disk.

Figure 2 presents a stacked area chart for dust mass and indicates that fifteen percent of the total dust ( $\sim 1.5 M_{\text{Jup}}$ ) is ejected from the stellar system. Observations at mm wavelengths show that the dust opacity spectral index is around or smaller than unity in the envelopes of Class 0 and I objects (e.g., Kwon et al. 2009; Chiang et al. 2012; Miotello et al. 2014; Galametz et al. 2019), whereas it is  $\sim 1.7$  in the interstellar medium (Finkbeiner et al. 1999; Li & Draine 2001). These observations suggest the presence of grown dust grains larger than  $1 \mu\text{m}$  in the envelope at an early stage of star formation. Such dust grains are likely supplied by the outflow from the disk (Wong et al. 2016; Tsukamoto et al. 2021) rather than being formed in situ (Ormel et al. 2009), due to short timescales of  $\sim 10^5$  years. Our results imply that not only the outflow but also the ejection can transport grown dust grains to the envelope.

Figure 3 illustrates the radial distributions of various properties of gas and dust grains. In the left column, the surface densities of gas, grown dust, and small dust are displayed, allowing a quantitative comparison of their magnitudes. For example, panel i-a shows a gradual increase in the gas density toward the center from 1000 to 80 au, indicating the presence of the accretion envelope. A significant order-of-magnitude increase in gas density is observed at 80 au, defining the outer boundary of the disk. The transition between the envelope and the disk is characterized by a shift in dominant dust components; the envelope contains primarily small dust, whereas the disk is rich in grown dust grains. Panels i-a and i-b show that, at 20 and 50 kyr, the gas surface density is approximately equal to 100 times the surface density of grown dust in the inner regions, and 100 times the surface density of small dust in the outer regions. By the epoch of 130 kyr (panel i-c), a discrepancy emerges between the gas and grown dust distributions within a radius of 100 au. This difference becomes more prominent at 300 kyr (panel i-d), where the surface density of the grown dust exhibits a peak at around 30 au. The dust-to-gas mass ratio exceeds the conventional value of  $10^{-2}$  within such a "dust ring". At 300 kyr, there is a depletion of dust grains due to their radial drift motion, resulting in the total dust mass (summing up the grown and small components) being  $0.76 \times 10^{-2}$  of the gas mass within 1000 au, despite their comparable masses up to 130 kyr.

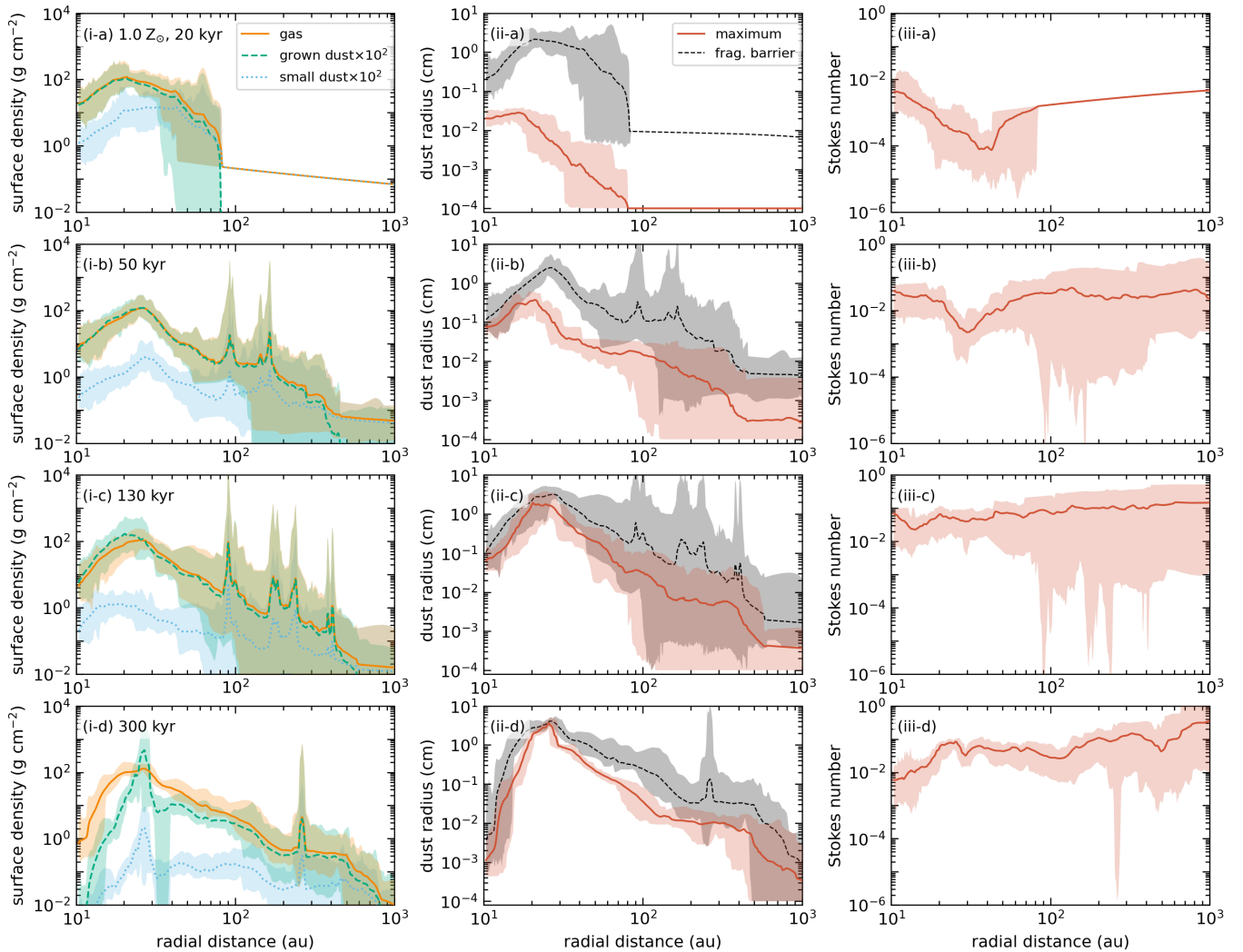


**Fig. 3.** Evolution of the radial distributions of the gas and dust for the case of  $1.0 Z_{\odot}$ . Each column shows the radial profiles of the surface densities (left), the maximum dust size (middle), and the Stokes number (right) at the same epochs as in Figure 1. The lines provide the azimuthally averaged values, and the shaded layers show the ranges of variation of these values at a given radius, with the upper and lower boundaries corresponding to the maximum and minimum values. In the left panels, the orange, green, and blue colors represent different components: gas, grown dust, and small dust, respectively. The densities of grown and small dust are multiplied by 100 to make comparisons easier. In the middle panels, the lines depict the maximum dust size (red solid line) and the fragmentation barrier given by Equation (15) (black dashed line).

The dust ring is created by accumulation of radially drifting dust at a gas pressure bump. In a disk that is gravitationally unstable, the transport of angular momentum is more effective in the outer regions, where the gravitational instability is most pronounced, and becomes less effective towards the inner regions. As the efficiency of angular momentum transport varies with distance from the center, gas flowing towards the center piles up in an innermost region of the disk, leading to the formation of a pressure bump. This phenomenon, known as the "bottleneck effect," has been extensively studied by Vorobyov et al. (2023). We note that the dust ring is at a radial position where the efficiency of angular momentum transport (i.e., gravitational and viscous torque) takes a minimum, which depends on the phenomenological  $\alpha$  parameter. Additionally, its position may also depend on the sink radius, with a smaller sink radius causing the dust ring to shift inward (see Vorobyov et al. 2023 for more details).

The middle panels in Figure 3 demonstrate efficient dust growth within the disk, where the maximum dust size is sig-

nificantly larger than in the surrounding envelope. We find that the dust size grows to mm scale at an early stage, reaching 0.1 to 1.0 mm within 100 au at 50 kyr (panel ii-b). The timescale for the collisional dust growth from micron to mm radii is given by (Birnstiel et al. 2016)

$$t_{\text{growth}} \simeq \left( \frac{\Sigma_{\text{d}}}{\Sigma_{\text{g}}} \right)^{-1} \frac{1}{\Omega_{\text{K}}} \sim 20 \left( \frac{\Sigma_{\text{d}}/\Sigma_{\text{g}}}{10^{-2}} \right)^{-1} \left( \frac{M_{*}}{0.5 M_{\odot}} \right)^{-1/2} \left( \frac{r}{100 \text{ au}} \right)^{3/2} \text{ kyr}. \quad (19)$$

Note that collisions between dust grains of equal size are assumed in the above estimate, as used in our dust growth scheme. Our results are consistent with this timescale. After 50 kyr, the dust size nearly reaches a plateau of growth (panels ii-c and ii-d). Except in the innermost regions, the fact that the maximum dust size stays below the fragmentation barrier suggests that the drift barrier (i.e., radial drift) determines the dust size.

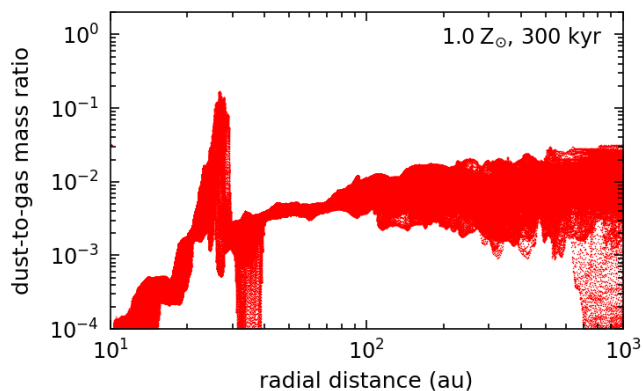


**Fig. 4.** Variation in the dust-to-gas mass ratio from the canonical value in the case of  $1.0 Z_{\odot}$  at 300 kyr. The red dots represent the dust-to-gas mass ratios for each grid cell.

The Stokes number increases with the growth of dust grains. In Figure 3, panel iii-a shows that in the early stages, the Stokes number varies from  $10^{-2}$  to  $10^{-4}$  within the disk. As dust grows further, the Stokes number reaches around 0.1 throughout the disk. The lower Stokes number in the early stages is not only due to the small size of dust grains but also to the high density and temperature commonly observed in young disks (Vorobyov et al. 2024). Moreover, the dust ring exhibits a high dust-to-gas mass ratio and a Stokes number exceeding 0.01, indicating the potential occurrence of streaming instability in this region. We will further discuss this possibility later in Section 4.

Figure 4 presents the variation of the dust-to-gas mass ratio at the epoch of 300 kyr. We see that the dust-to-gas mass ratio is as high as  $\sim 0.1$  at the dust ring, whose radius is approximately 30 au. In the outer part of the ring within  $\sim 100$  au, the dust-to-gas mass ratio is slightly smaller than the initial value 0.01, suggesting that some grains have drifted inward to be trapped by the dust ring. Moving even further out beyond 100 au, there are large scatters due to the gravitational instability and turbulent motion in that region. However, the scatters are insufficient to alter the thermal conditions of the gas and, consequently, the strength of the disk fragmentation. Throughout the evolution, we observe almost the same level of disk fragmentation as in the case where we ignore the dust growth and drifting motion apart from the gas.

### 3.2. Low metallicities

We describe our simulation results for the low-metallicity cases with 0.1 and 0.01  $Z_{\odot}$  in Sections 3.2.1 and 3.2.2, respectively. In particular, we study disk evolution and dust growth at these metallicities, focusing on their differences from the solar-metallicity case.

#### 3.2.1. One tenth of solar metallicity

Figure 5 shows the evolution of the disk at 0.1  $Z_{\odot}$ . It can be observed from the left panels that the outer radius of the disk expands over time, reaching approximately 600 au by the last epoch at 300 kyr. Disk fragmentation is evident, particularly at 130 kyr, where fragmentation is intense with  $\sim 10$  clumps present in the disk (panel i-c). At 300 kyr, the disk fragmentation diminishes (but gravitational instability persists), with only one clump remaining (panel i-d). The evolution of the disk up

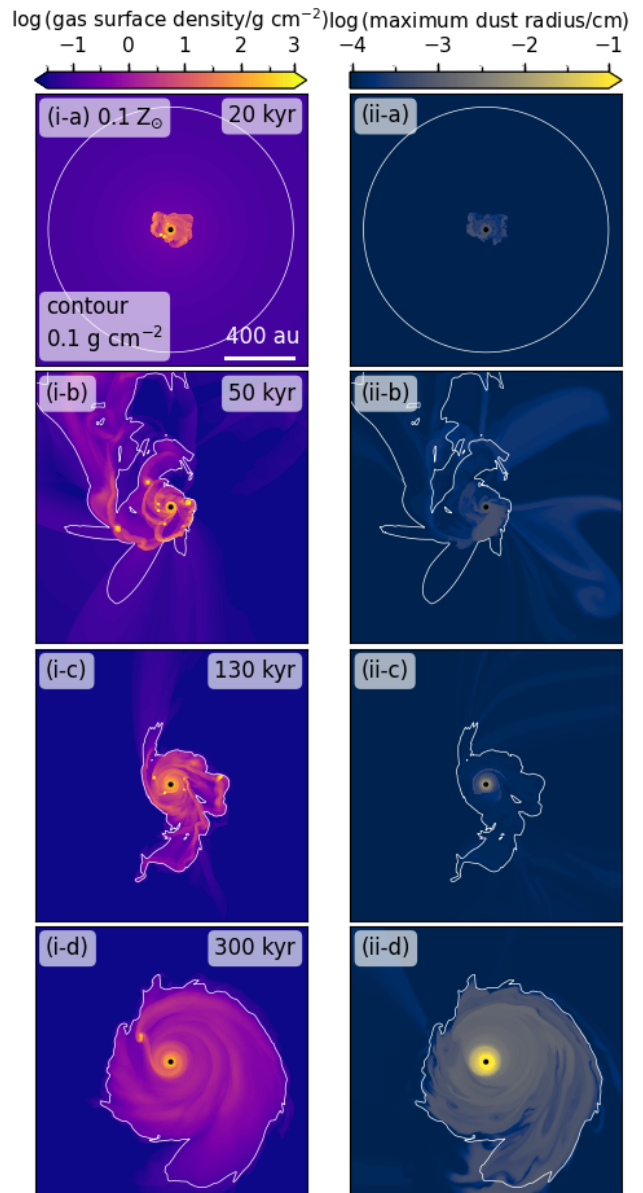


**Fig. 5.** Same as Figure 1 but for the case of 0.1  $Z_{\odot}$ .

to this epoch closely resembles that of the solar-metallicity disk, as shown in Figure 1. The similarity in the disk evolution at 1.0 and 0.1  $Z_{\odot}$  has been also reported by previous studies that investigated the metallicity dependence of the disk fragmentation (See Tanaka & Omukai 2014 for an analytic study; Machida & Nakamura 2015; Bate 2014, 2019; Vorobyov et al. 2020a; Matsukoba et al. 2022 for numerical studies). Our results support their findings.

Our simulation for the case with 0.1  $Z_{\odot}$  shows two ejection events: one occurring at 20 kyr (shortly after the epoch of panel i-a) and the other at 70 kyr. In panel i-b, the regions that extend from the center to the upper left, where the density exceeds  $0.1 \text{ g cm}^{-2}$ , provide evidence of the first ejection event at 20 kyr. Similarly to the case with solar metallicity, the ejection events

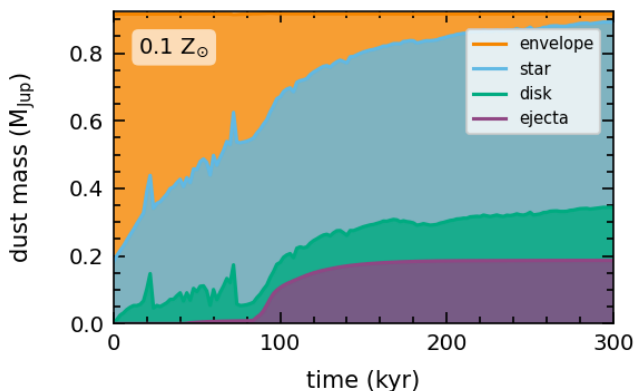


**Fig. 6.** Same as Figure 2 but for the cases of  $0.1 Z_{\odot}$ .

are triggered by close encounters between clumps, and a portion of the ejected material escapes from the stellar system.

In Figure 5, panels ii-a and ii-b indicate that the largest dust size present in all areas is approximately  $10^{-4}$  cm, showing no indications of dust growth. By 130 kyr (panel ii-c), the grown dust grains appear only in an innermost part of the disk (around 10–20 au), although the maximum dust size remains at  $10^{-4}$  cm across the entire disk. The spatial distribution of the maximum dust size dramatically changes at 300 kyr (panel ii-d), with dust growth evident throughout the disk. In the outer part of the disk, the maximum dust size eventually reaches  $\sim 10^{-3}$  to  $10^{-2}$  cm. This contrasts to the case with  $1.0 Z_{\odot}$ , where the disk becomes filled with dust grains  $\geq 10^{-2}$  cm much earlier. Furthermore, unlike the case with  $1.0 Z_{\odot}$ , the maximum dust size within the envelope remains at  $\sim 10^{-4}$  cm at all periods, indicating the absence of grown dust. This is because the maximum dust size within the disk remains small during ejection events at 20 kyr and 70 kyr, preventing the transport of large dust grains to the envelope through ejection.

Figure 6 presents a stacked area chart of the dust mass for the case of  $0.1 Z_{\odot}$ , revealing that dust grains with a mass equivalent to one-fifth of the initial cloud ( $0.2 M_{\text{Jup}}$ ) are ejected from the system. Most of the ejecta are provided by the event at 70 kyr. As evident from Figure 5, dust size growth is hardly progressed by the time of the ejection events. Therefore, only small dust grains, not grown dust grains, are scattered into the surrounding envelope by ejection events, unlike in the case of solar metallicity.

The left panels in Figure 7 compares the surface densities of gas, grown dust, and small dust at the metallicity of  $0.1 Z_{\odot}$ . As shown in panels i-a and i-b, at  $0.1 Z_{\odot}$ , the surface density of the grown dust tends to be similar to or slightly lower than that of the small dust until 50 kyr. By 130 kyr (panel i-c), within a radius of 50 au, the surface density of the grown dust exceeds that of the small dust. Later at 300 kyr (panel i-d), the grown dust becomes the dominant component throughout the disk. Recall that, in the case of solar metallicity, the surface density of the grown dust is always greater than that of the small dust (Figure 3). These results indicate that at the metallicity of  $0.1 Z_{\odot}$ , dust growth in the disk progresses at a slower rate.

Substituting the dust-to-gas mass ratio  $\Sigma_{\text{d}}/\Sigma_{\text{g}} = 10^{-3}$  into Equation (19), we estimate the dust growth timescale at  $0.1 Z_{\odot}$  as  $\sim 200$  kyr. In this study, we have followed such a long-term evolution over a period of 300 kyr, comparable to this timescale. This marks the first time that such long-term simulations of dust growth in a low-metallicity disk have been performed alongside

the formation and global evolution of the disk. Indeed, our simulation shows that the dust growth finally occurs after  $\geq 100$  kyr long-term evolution in a  $0.1 Z_{\odot}$  disk.

Panel i-d in Figure 7 indicates that the surface density of grown dust has a spike at  $\sim 15$  au, similar to the case with solar metallicity. This spike represents a ring-like structure, which is confirmed by the spatial distribution of grown dust. This dust ring is also formed by dust accumulation at a gas-pressure bump produced by the bottleneck effect.

Despite slower dust growth at  $0.1 Z_{\odot}$  compared to the case with  $1.0 Z_{\odot}$ , our simulation results suggest that the timing of the dust ring formation does not change. With solar metallicity, by 130 kyr, dust grains sufficiently grow to a cm scale. Therefore, the first dust ring is formed at an early stage,  $\sim 80$  kyr. However, since the disk is still gravitationally unstable at this period, clumps formed by gravitational instability orbit at radii outside the dust ring ( $\sim 200$  au), destroying it. Subsequently, these clumps migrate inwards and are eventually dispersed by tidal forces from the central star. Dust grains from the dispersed clumps are distributed to the surrounding area, forming a new dust ring from these grains (Vorobyov & Elbakyan 2019). In the disk with solar metallicity, this cycle of dust ring formation and destruction is repeated, and a long-lasting dust ring is finally formed  $\sim 300$  kyr, when the disk fragmentation diminishes. In the disk with  $0.1 Z_{\odot}$ , since the dust growth timescale is similar to the timescale of the disk stabilization, the first dust ring is formed  $\sim 230$  kyr and is maintained. This process results in density profiles with similar characteristics for both metallicities.

Slow dust growth at  $0.1 Z_{\odot}$  is also apparent in the middle panels in Figure 7. Panels ii-a and ii-b show that the maximum dust size is less than  $10^{-3}$  cm in the inner disk at 20 and 50 kyr. By 130 kyr (panel ii-c), the size reaches approximately  $10^{-2}$  cm near 10 au but remains at  $10^{-4}$  cm beyond 100 au, indicating minimal dust growth in those regions. At 300 kyr (panel ii-d), an overall dust growth is observed, with a maximum size of  $10^{-2}$  to  $10^{-3}$  cm around 100 au, regions where growth is limited in earlier epochs.

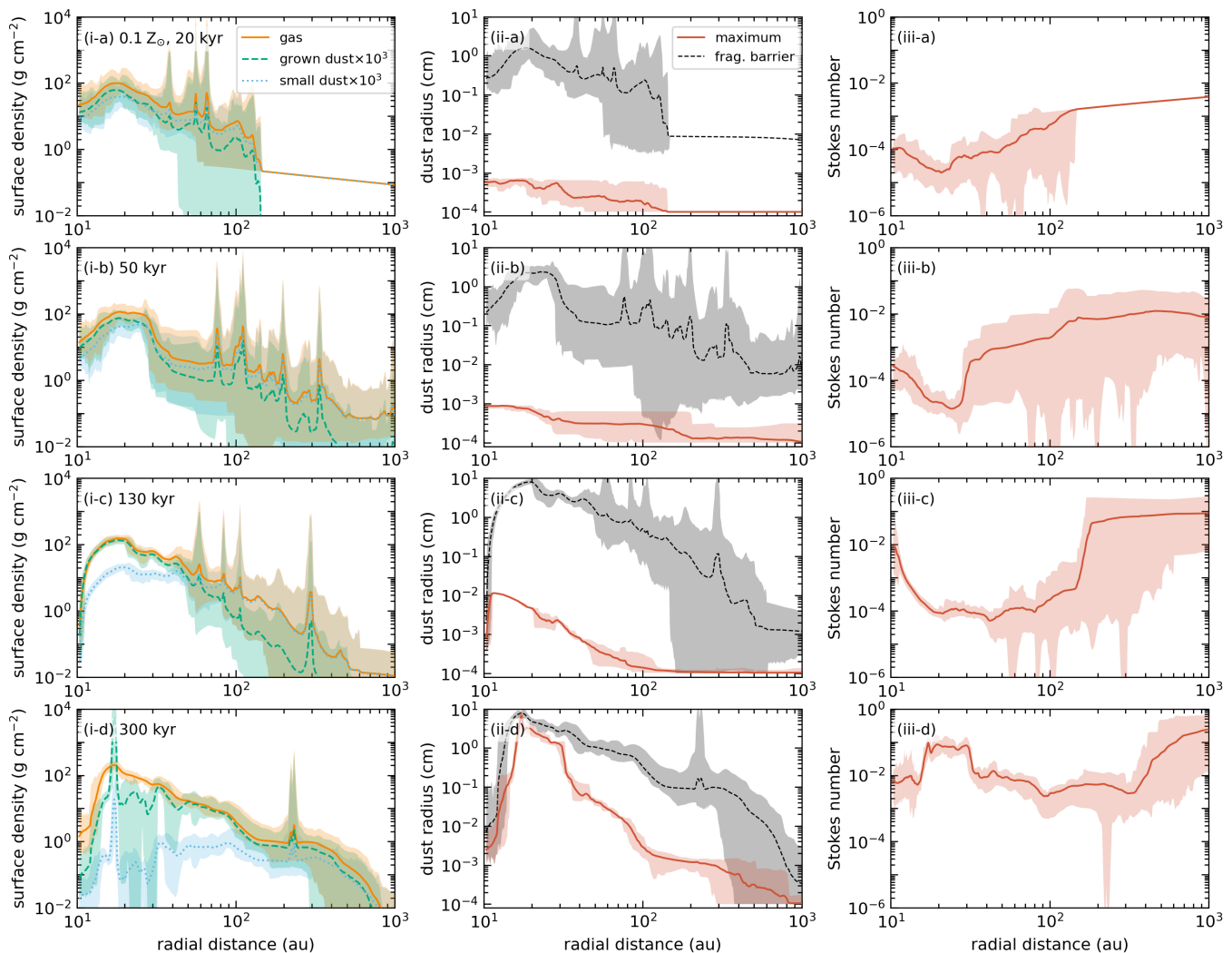
As shown in the right panels in Figure 7, the Stokes number in the early phase of the disk tends to be smaller than that at the solar metallicity, because of the slower dust growth. For example, at a position of 100 au after 130 kyr of disk formation (panel iii-c), the Stokes number is at  $10^{-4}$ , three orders of magnitude smaller than that of the solar-metallicity case. At 300 kyr when dust growth becomes significant (panel iii-d), the Stokes number in the disk region ( $\sim 400$  au) increases, ranging between  $10^{-3}$  and 0.1.

Finally, Figure 8 shows that the dust-to-gas mass ratio in the dust ring is much greater than the canonical value of 0.001, increasing by two orders of magnitude to a maximum of 0.1. The magnitude of dust concentration is therefore comparable to that of the solar metallicity case, see Figure 4, but the ring in this case is notably narrower. These high dust-to-gas mass ratios, together with the Stokes number exceeding 0.01, indicate that the ring may be prone to develop the streaming instability. On the other hand, the dust-to-gas ratio in the  $0.1 Z_{\odot}$  disk beyond 70 au features little variations, unlike the  $1.0 Z_{\odot}$  case, indicating that dust dynamics in the lower metallicity is weakly perturbed by local pressure variations in the gravitationally unstable disk.

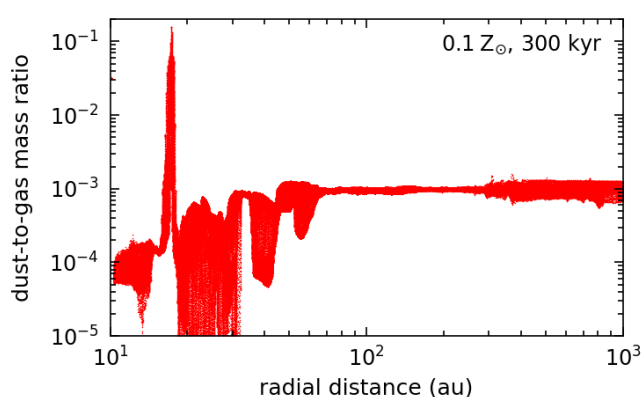
### 3.2.2. One hundredth of solar metallicity

Figure 9 demonstrates that the disk evolution at the metallicity of  $0.01 Z_{\odot}$  is distinctly different from the other two cases with  $1.0$  and  $0.1 Z_{\odot}$ . In this model, the most intense fragmentation occurs





**Fig. 7.** Same as Figure 3 but for the case of  $0.1 Z_{\odot}$ . The densities of the grown and small dust grains are multiplied by a factor of  $10^3$  to facilitate their comparison with the gas density.



**Fig. 8.** Same as Figure 4 but for the case of  $0.1 Z_{\odot}$ .

at 20 kyr (panel i-a). Afterward, the disk quickly becomes gravitationally stable, and at 130 kyr (panel i-c), which represents the most unstable moment for the other models, the disk is com-

pletely stable, with both gas and dust having an axisymmetric surface density structure.

At  $0.01 Z_{\odot}$ , the disk evolution proceeds more rapidly than the other models. This is attributed to higher gas temperatures in the envelope resulting from inefficient dust thermal emission induced by mutual collisions with gas molecules. The higher temperature of the envelope leads to rapid gas accretion from the envelope to the disk, which is approximately given by

$$\dot{M}_{\text{env}} \simeq \frac{M_{\text{Jeans}}}{t_{\text{ff}}} \simeq \frac{c_s^3}{G} \propto T^{3/2}, \quad (20)$$

where  $M_{\text{J}} = 4/3\pi\rho(l_{\text{Jeans}}/2)^3$  is the Jeans mass,  $l_{\text{Jeans}} = \sqrt{\pi c_s^2 / (G\rho)}$  is the Jeans length, and  $t_{\text{ff}} = \sqrt{3\pi / (32G\rho)}$  is the free-fall time (Shu 1977; Stahler et al. 1986). Since the initial cloud mass for each model is fixed at  $\approx 0.9 M_{\odot}$ , under high accretion rates, the gas supply from the envelope to the disk concludes in an earlier phase, thereby leading to faster disk stabilization.

The panels in the right column of Figure 9 indicate that at  $0.01 Z_{\odot}$  the dust size remains constant at  $10^{-4}$  cm in both the disk and the surrounding envelope. By 130 kyr (panel ii-c), only

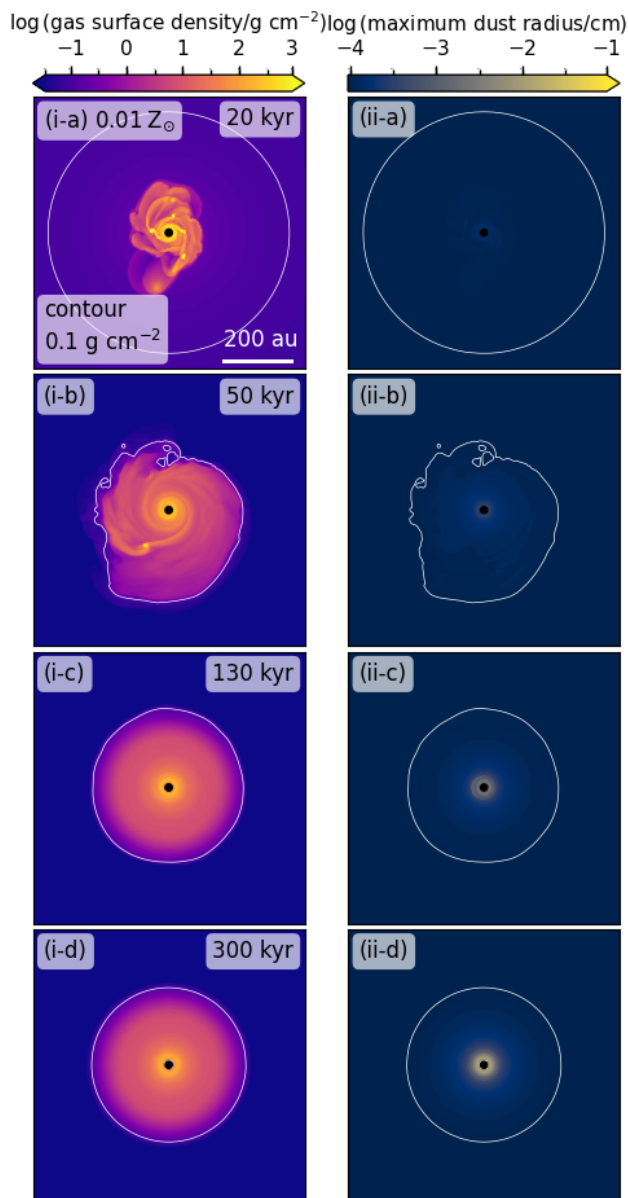


**Fig. 9.** Same as Figure 1 but for the case of  $0.01 Z_{\odot}$ .

the innermost region of the disk ( $\lesssim 50$  au) exhibits an increase in dust size to  $\sim 10^{-3}$  cm. Throughout the evolution until 300 kyr (panel ii-d), the region where dust size growth occurs does not expand, and the dust size only reaches  $10^{-2}$  cm in the innermost part of the disk. Unlike the higher-metallicity cases, mm-sized dust grains are not observed throughout the disk at  $0.01 Z_{\odot}$ .

We note that no ejection events are observed in the disk for this case. Figure 10 indicates that all the dust grains either accrete onto the central star or remain within the disk. In the case of  $0.01 Z_{\odot}$ , the shorter period of gravitational instability in the disk may contribute to making ejection events difficult.

The left panels in Figure 11 displays the surface-density radial profiles of gas, grown dust, and small dust at the metallicity of  $0.01 Z_{\odot}$ . At 20 kyr after disk formation (panel i-a), the surface density of the small dust is about an order of magnitude larger

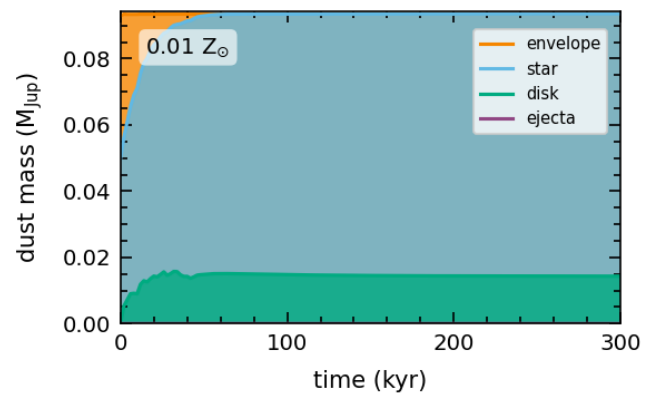


**Fig. 10.** Same as Figure 2 but for the cases of  $0.01 Z_{\odot}$ .

than that of the grown dust. Additionally, the surface density of the small dust multiplied by  $10^4$  is nearly equivalent to the gas surface density, with the entire disk having a dust-to-gas mass ratio of  $10^{-4}$ . At 50 kyr (panel i-b), the surface density of the grown dust becomes similar to that of small dust within an inner radius of 20 au. As time progresses to 130 kyr and 300 kyr (panels i-c and i-d), the grown dust becomes the dominant component within the radius of 50 au. However, beyond this radius, the surface density of the grown dust is always smaller than that of the small dust and does not reach  $10^{-4}$  of that of gas.

The panels in the middle column of Figure 11 indicate that the dust size does not grow much by the end of the simulation. According to panel ii-d, the maximum dust size in the innermost regions of the disk ( $\sim 20$  au) is  $\sim 10^{-2}$  cm, but it remains at  $\sim 10^{-4}$  cm  $\sim 100$  au. In contrast, we observe dust grains with mm scale in the cases of  $1.0$  and  $0.1 Z_{\odot}$ . This clearly indicates slower dust growth at  $0.01 Z_{\odot}$  compared to the higher metallicity cases. These results are attributed to the simulated time of disk evolution (300 kyr) being shorter than the dust growth timescale, which is  $\sim 2$  Myr, with the dust-to-gas mass ratio of  $10^{-4}$  (Equation 19). The dust growth timescale at  $0.01 Z_{\odot}$  is comparable to the lifetime of protoplanetary disks in nearby clusters,  $\sim 3$ – $6$  Myr (e.g., Haisch et al. 2001; Hernández et al. 2007; Mamajek 2009; Ribas et al. 2014). Furthermore, shorter disk lifetimes in low-metallicity environments have been suggested by observations (e.g., Yasui et al. 2010, 2016, 2021; Guarcello et al. 2021) and theories (Nakatani et al. 2018a,b; Georig et al. 2023). Therefore, the disk with the metallicity of  $0.01 Z_{\odot}$  may dissipate before dust grains can grow to mm in size. Panel iii-d in Figure 11 presents that the Stokes number at 300 kyr remains low at  $10^{-4}$  across most of the disk ( $\sim 20$ – $100$  au) due to the small dust sizes. This value is two to three orders of magnitude smaller than those in the higher-metallicity cases.

#### 4. Implications for planetesimal and planet formation

In the context of planet formation, how planetesimals are formed from mm- to cm-sized dust grains is an intriguing subject. The streaming instability is a promising pathway to planetesimal formation, as described in Section 1.

Several numerical studies examined dust clumping caused by streaming instability, utilizing the local shearing box approximation to model a small vertical slice of the protoplanetary disk (Carrera et al. 2015; Yang et al. 2017; Li & Youdin 2021; Lim et al. 2023). These studies explored a wide range of paramete-

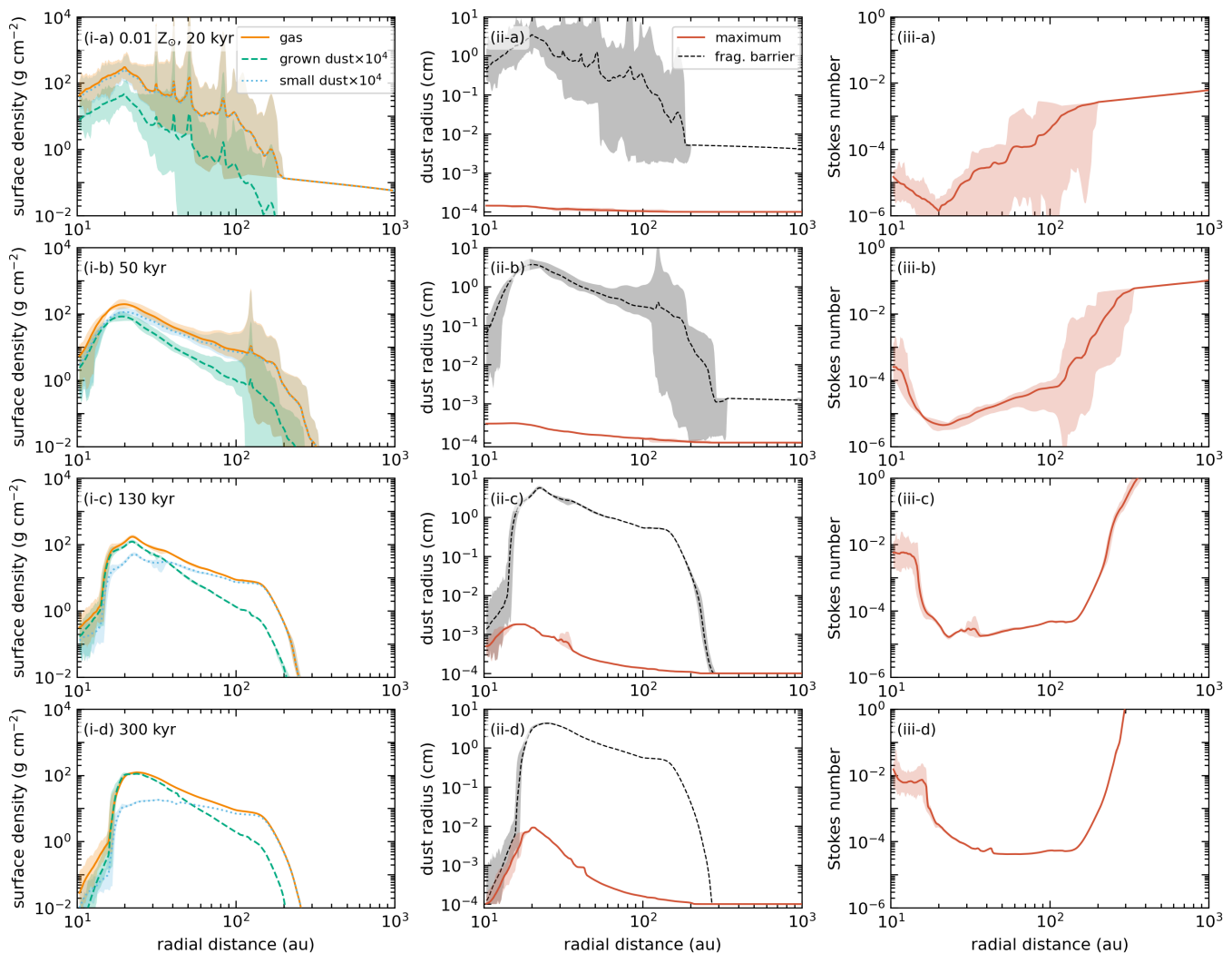


**Fig. 11.** Same as Figure 3 but for the case of  $0.01 Z_{\odot}$ . The densities of grown and small dust grains are multiplied by  $10^4$  to make the comparison with that of gas easier.

ters, including the dust-to-gas mass ratio and the Stokes number, and identified the critical dust-to-gas mass ratio as a function of the Stokes number. Beyond this critical ratio, the streaming instability leads to strong clumping and subsequent dust self-gravitational collapse. The critical value is found to be lowest in the range of Stokes numbers between 0.1 and 0.3, with the dust-to-gas mass ratio ranging from 0.002 to 0.01. Lim et al. (2023) also considered the effect of turbulent gas diffusion on dust concentration caused by streaming instability and provided a fitting formula for the critical ratio.

Dust rings with high surface densities facilitate dust growth and have a high dust-to-gas mass ratio, making them prone to the streaming instability and thus creating an ideal environment for planetesimal formation. To assess the potential for planetesimal formation in the dust rings observed in our simulations, we verify whether the grid cells within the dust ring regions meet the criterion identified by Lim et al. (2023). Figure 12 illustrates the distribution of grid cells from 10 to 40 au from the center, including the dust ring regions, on the Stokes number – dust-to-gas mass ratio plane at 300 kyr. The gray shaded area indicates regions where the planetesimal formation through the streaming instability is expected. The figure reveals that some

grid cells within this shaded area exist in the dust rings of both the metallicities. Therefore, we can anticipate planetesimal formation in both the dust rings. The total dust masses of grid cells that meet the critical dust-to-gas mass ratio are  $68 M_{\oplus}$  for  $1.0 Z_{\odot}$  and  $12 M_{\oplus}$  for  $0.1 Z_{\odot}$ . The hydrodynamic simulations of streaming instability (Simon et al. 2016; Abod et al. 2019) showed that the conversion efficiency from dust grains to planetesimals is approximately 50%, with variations depending on the radial pressure gradient and ranging from 10 to 80% (Abod et al. 2019). If a conversion efficiency of 50% is assumed, then the total planetesimal masses in the dust ring would be  $32 M_{\oplus}$  for  $1 Z_{\odot}$  and  $6 M_{\oplus}$  for  $0.1 Z_{\odot}$ .

Liu et al. (2019) examined protoplanet formation from planetesimals formed through streaming instability in a dust ring by conducting N-body simulations. In their simulations, planetesimals grow through mutual collisions with other planetesimals, i.e., planetesimal accretion, and through pebble accretion. The initial size distribution of planetesimals, formed by streaming instability, is described by a single power law (Simon et al. 2016, 2017) and exhibits exponential decay at the high-mass end (Schäfer et al. 2017). Liu et al. (2019) found that the largest planetesimal initially grows by planetesimal accretion,

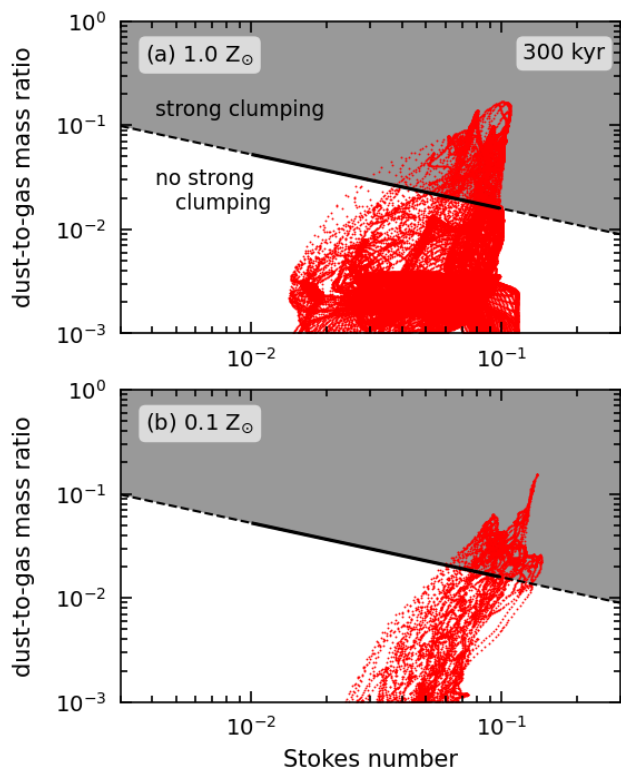


**Fig. 12.** Possibility of planetesimal formation by streaming instability at 300 kyr. The red points represent the grid cells from 10 to 40 au from the center, including the dust ring regions. Each panel displays two different metallicities:  $1.0 Z_{\odot}$  (upper panel) and  $0.1 Z_{\odot}$  (lower panel). The black solid line depicts the critical dust-to-gas mass ratio as a function of the Stokes number provided by Lim et al. (2023), above which dust concentration induced by streaming instability can trigger planetesimal formation. Since the range of the Stokes number explored in their study is from 0.01 to 0.1, we extrapolate the solid line and represent this extrapolation with the dashed line.

and then once its mass reaches  $10^{-2} M_{\oplus}$ , pebble accretion becomes more efficient than planetesimal accretion. Eventually, a rocky protoplanet with a mass of  $1 M_{\oplus}$  can form within 1 Myr. They assumed the radial position of the dust ring is 2.7 au, corresponding to the snow line for water ice. However, our dust rings are located far from the snow line. Since the efficiencies of planetesimal and pebble accretions decrease with radial distance (Ormel et al. 2010 for protoplanet accretion; Visser & Ormel 2016 for pebble accretion), protoplanet formation becomes more challenging. For example, the timescale for runaway planetesimal accretion is  $\sim 1$  Myr at 20–30 au, similar to the gas disk’s lifetime. This suggests that the gas disk may disperse before a growing planetesimal reaches  $10^{-2} M_{\oplus}$ , preventing the switch to pebble accretion. Additionally, protoplanet formation in the disk with  $0.1 Z_{\odot}$  would be more difficult than in that with  $1.0 Z_{\odot}$ , due to a reduced dust budget for pebble accretion. We note that a dust ring, formed by the bottleneck effect, appears at a radius where the efficiency of angular momentum transport is minimal. Consequently, its position may depend on the magnitude of alpha viscosity or the sink radius. A dust ring may form at smaller radii with other parameter values, and protoplanet formation may be allowed even in a low-metallicity disk.

As shown in Figures 9 and 11, in the case of metallicity  $0.01 Z_{\odot}$ , dust growth is slow, and dust accumulation does not occur. Therefore, forming planetesimals through streaming insta-

bility is disadvantaged in the disk with  $0.01 Z_{\odot}$ . Another mechanism for the planet formation is disk fragmentation caused by gravitational instability (Boss 1998; Rice et al. 2003; Mayer et al. 2007; Kratter et al. 2010; Machida et al. 2011; Zhu et al. 2012; Vorobyov 2013; Tsukamoto et al. 2015; Nayakshin 2017a; Stamatellos & Inutsuka 2018; Vorobyov & Elbakyan 2018). Numerical and analytical studies examined the formation of gas giant planets through gravitational instability in a protoplanetary disk with low metallicity (Boss 2002; Matsuo et al. 2007; Meru & Bate 2010; Vorobyov et al. 2020a; Matsukoba et al. 2023 but see also Cai et al. 2006). In particular, Matsukoba et al. (2023) conducted numerical simulations of disk evolution over a long period (until 1 Myr after disk formation) at a metallicity of  $0.1 Z_{\odot}$  and found a gas giant planet that survives until the end of simulations. In the results for metallicity  $0.01 Z_{\odot}$  in this study, all fragments fall into the central star, but depending on the initial conditions, some fragments may survive. For instance, increasing the strength of gas-cloud rotation to enlarge the disk’s radius may make it less likely for fragments formed far from the center to fall into the central star.

## 5. Summary

We have investigated dust growth in a protoplanetary disk by performing two-dimensional radiation-hydrodynamic simulations, following long-term evolution for 300 kyr since the disk formation. Our code solves the dust-size growth and considers the dust motion separately from the gas, leading to non-uniform structures in the dust-to-gas mass ratio. Our simulations include three models with different initial dust-to-gas mass ratios:  $10^{-2}$ ,  $10^{-3}$ , and  $10^{-4}$ . We specifically focus on the dependence of dust growth on these ratios. Our findings are summarized as follows:

1. In the disk with the metallicity of  $1.0 Z_{\odot}$  (dust-to-gas mass ratio of  $10^{-2}$ ), dust size growth is more efficient in the disk region than in the surrounding envelope due to the higher density and temperature, which lead to increased growth rates. The size of dust exceeds  $10^{-2}$  cm after 50 kyr of disk formation at  $< 200$  au, consistent with the estimated timescale for dust size growth. The drift motion of grown dust grains results in a spatially non-uniform distribution of the dust-to-gas mass ratio. However, the deviation from the canonical values is not significant enough to affect the overall evolution of the disk.
2. In the disk with the metallicity of  $0.1 Z_{\odot}$  (dust-to-gas mass ratio of  $10^{-3}$ ), the growth rate of dust size is proportional to the dust density; hence, dust-size growth is slower compared to that at the metallicity of  $1.0 Z_{\odot}$ . At this metallicity, the timescale for dust growth at the disk scale ( $\sim 100$  au) is  $\sim 200$  kyr. Once the disk age reaches this timescale, the dust size within the disk becomes  $> 10^{-2}$  cm, akin to distributions at the metallicity of  $1.0 Z_{\odot}$ . The variation from the canonical dust-to-gas mass ratio is less pronounced than in the case of  $1.0 Z_{\odot}$ , and similarly, the overall evolution of the disk remains unaffected by dust growth.
3. In the disk with the metallicity of  $0.01 Z_{\odot}$  (dust-to-gas mass ratio of  $10^{-4}$ ), dust size growth is observed only in the innermost regions ( $\sim 20$  au). At a scale of 100 au, the dust size remains  $\sim 10^{-4}$  cm. The timescale for dust growth at this metallicity is  $\sim 2$  Myr, which is comparable to the lifetime of the gas disk. Therefore, the gas disk may dissipate before the dust grains can grow to mm sizes.
4. The dust ring forms in cases with metallicities of 1.0 and  $0.1 Z_{\odot}$ . Within this ring, the dust density is enhanced, which

facilitates dust growth, allowing dust size to exceed 1.0 cm. Additionally, the Stokes number reaches 0.1. Such situations are conducive to streaming instability, planetesimals may be formed.

In this paper, we have discussed the growth of dust size across the disk. To perform high-resolution calculations at the 100 au scale, we have introduced a sink cell of 10 au at the center of the computational domain. Since dust size growth is more rapid in the inner regions, conducting calculations that resolve smaller radii allows us to observe dust size growth even in a disk with low metallicity. For instance, at a dust-to-gas mass ratio of  $10^{-4}$ , the timescale for dust size growth at a radius of 1 au is estimated to be 10 kyr. The growth of dust size on these smaller scales will be discussed in future studies.

*Acknowledgements.* This research could never be accomplished without the support by Grants-in-Aid for Scientific Research (TH: 19H01934, 19KK0353, 21H00041) from the Japan Society for the Promotion of Science. E.I.V. acknowledges support by the Ministry of Science and Higher Education of the Russian Federation (State assignment in the field of scientific activity 2023, GZ0110/23-10-IF). Numerical computations were carried out on Cray XC50 at the Center for Computational Astrophysics (CfCA) of the National Astronomical Observatory of Japan and the Vienna Scientific Cluster (VSC-4).

## References

- Abod, C. P., Simon, J. B., Li, R., et al. 2019, *ApJ*, 883, 192
- Adachi, I., Hayashi, C., & Nakazawa, K. 1976, *Progress of Theoretical Physics*, 56, 1756
- Akeson, R. L., Chen, X., Ciardi, D., et al. 2013, *PASP*, 125, 989
- Basu, S. 1997, *ApJ*, 485, 240
- Basu, S. & Vorobyov, E. I. 2012, *ApJ*, 750, 30
- Bate, M. R. 2009, *MNRAS*, 392, 590
- Bate, M. R. 2014, *MNRAS*, 442, 285
- Bate, M. R. 2019, *MNRAS*, 484, 2341
- Binney, J. & Tremaine, S. 1987, *Galactic dynamics* (Princeton: Princeton University Press)
- Birnstiel, T., Fang, M., & Johansen, A. 2016, *Space Sci. Rev.*, 205, 41
- Birnstiel, T., Klahr, H., & Ercolano, B. 2012, *A&A*, 539, A148
- Blum, J. 2018, *Space Sci. Rev.*, 214, 52
- Boss, A. P. 1998, *ApJ*, 503, 923
- Boss, A. P. 2002, *ApJ*, 567, L149
- Cai, K., Durisen, R. H., Michael, S., et al. 2006, *ApJ*, 636, L149
- Carrera, D., Johansen, A., & Davies, M. B. 2015, *A&A*, 579, A43
- Carrera, D. & Simon, J. B. 2022, *ApJ*, 933, L10
- Chiang, H.-F., Looney, L. W., & Tobin, J. J. 2012, *ApJ*, 756, 168
- Colella, P. & Woodward, P. R. 1984, *Journal of Computational Physics*, 54, 174
- Drążkowska, J., Bitsch, B., Lambrechts, M., et al. 2023, in *Astronomical Society of the Pacific Conference Series*, Vol. 534, *Protostars and Planets VII*, ed. S. Inutsuka, Y. Aikawa, T. Muto, K. Tomida, & M. Tamura, 717
- Finkbeiner, D. P., Davis, M., & Schlegel, D. J. 1999, *ApJ*, 524, 867
- Galamez, M., Maury, A. J., Valdivia, V., et al. 2019, *A&A*, 632, A5
- Gehrig, L., Steindl, T., Vorobyov, E. I., Guadarrama, R., & Zwintz, K. 2023, *A&A*, 669, A84
- Goldreich, P. & Ward, W. R. 1973, *ApJ*, 183, 1051
- Guarcello, M. G., Biazzo, K., Drake, J. J., et al. 2021, *A&A*, 650, A157
- Haghighipour, N. & Boss, A. P. 2003, *ApJ*, 583, 996
- Haisch, Karl E. J., Lada, E. A., & Lada, C. J. 2001, *ApJ*, 553, L153
- Hayashi, C. 1981, *Progress of Theoretical Physics Supplement*, 70, 35
- Henderson, C. B. 1976, *AIAA Journal*, 14, 707
- Hernández, J., Hartmann, L., Megeath, T., et al. 2007, *ApJ*, 662, 1067
- Hosokawa, T. & Omukai, K. 2009, *ApJ*, 703, 1810
- Johansen, A., Oishi, J. S., Mac Low, M.-M., et al. 2007, *Nature*, 448, 1022
- Johansen, A. & Youdin, A. 2007, *ApJ*, 662, 627
- Johansen, A., Youdin, A., & Klahr, H. 2009, *ApJ*, 697, 1269
- Kratter, K. M., Murray-Clay, R. A., & Youdin, A. N. 2010, *ApJ*, 710, 1375
- Kutra, T., Wu, Y., & Qian, Y. 2021, *AJ*, 162, 69
- Kwon, W., Looney, L. W., Mundy, L. G., Chiang, H.-F., & Kemball, A. J. 2009, *ApJ*, 696, 841
- Li, A. & Draine, B. T. 2001, *ApJ*, 554, 778
- Li, R. & Youdin, A. N. 2021, *ApJ*, 919, 107
- Lim, J., Simon, J. B., Li, R., et al. 2023, *arXiv e-prints*, arXiv:2312.12508
- Liu, B., Ormel, C. W., & Johansen, A. 2019, *A&A*, 624, A114
- Machida, M. N., Inutsuka, S.-i., & Matsumoto, T. 2011, *ApJ*, 729, 42
- Machida, M. N. & Nakamura, T. 2015, *MNRAS*, 448, 1405
- Mamajek, E. E. 2009, in *American Institute of Physics Conference Series*, Vol. 1158, *Exoplanets and Disks: Their Formation and Diversity*, ed. T. Usuda, M. Tamura, & M. Ishii, 3–10
- Matsukoba, R., Tanaka, K. E. I., Omukai, K., Vorobyov, E. I., & Hosokawa, T. 2022, *MNRAS*, 515, 5506
- Matsukoba, R., Vorobyov, E. I., Hosokawa, T., & Guedel, M. 2023, *MNRAS*, 526, 3933
- Matsuo, T., Shibai, H., Ootsubo, T., & Tamura, M. 2007, *ApJ*, 662, 1282
- Mayer, L., Lufkin, G., Quinn, T., & Wadsley, J. 2007, *ApJ*, 661, L77
- Meru, F. & Bate, M. R. 2010, *MNRAS*, 406, 2279
- Miotello, A., Testi, L., Lodato, G., et al. 2014, *A&A*, 567, A32
- Molyarova, T., Vorobyov, E. I., Akimkin, V., et al. 2021, *ApJ*, 910, 153
- Mulders, G. D., Pascucci, I., Apai, D., Frasca, A., & Molenda-Zakowicz, J. 2016, *AJ*, 152, 187
- Nakatani, R., Hosokawa, T., Yoshida, N., Nomura, H., & Kuiper, R. 2018a, *ApJ*, 857, 57
- Nakatani, R., Hosokawa, T., Yoshida, N., Nomura, H., & Kuiper, R. 2018b, *ApJ*, 865, 75
- Nayakshin, S. 2017a, *MNRAS*, 470, 2387
- Nayakshin, S. 2017b, *PASA*, 34, e002
- Omukai, K., Tsuribe, T., Schneider, R., & Ferrara, A. 2005, *ApJ*, 626, 627
- Ormel, C. W., Dullemond, C. P., & Spaans, M. 2010, *ApJ*, 714, L103
- Ormel, C. W., Paszun, D., Dominik, C., & Tielens, A. G. G. M. 2009, *A&A*, 502, 845
- Petigura, E. A., Marcy, G. W., Winn, J. N., et al. 2018, *AJ*, 155, 89
- Ribas, Á., Merín, B., Bouy, H., & Maud, L. T. 2014, *A&A*, 561, A54
- Rice, W. K. M., Armitage, P. J., Bate, M. R., & Bonnell, I. A. 2003, *MNRAS*, 339, 1025
- Safronov, V. S. 1972, *Evolution of the protoplanetary cloud and formation of the earth and planets*. (Jerusalem: Keter Publishing House)
- Santos, N. C., Israelian, G., & Mayor, M. 2004, *A&A*, 415, 1153
- Schäfer, U., Yang, C.-C., & Johansen, A. 2017, *A&A*, 597, A69
- Shu, F. H. 1977, *ApJ*, 214, 488
- Simon, J. B., Armitage, P. J., Li, R., & Youdin, A. N. 2016, *ApJ*, 822, 55
- Simon, J. B., Armitage, P. J., Youdin, A. N., & Li, R. 2017, *ApJ*, 847, L12
- Stahler, S. W., Palla, F., & Salpeter, E. E. 1986, *ApJ*, 302, 590
- Stamatellos, D. & Inutsuka, S.-i. 2018, *MNRAS*, 477, 3110
- Stamatellos, D. & Whitworth, A. P. 2009, *MNRAS*, 392, 413
- Stone, J. M. & Norman, M. L. 1992, *ApJS*, 80, 753
- Stoyanovskaya, O. P., Okladnikov, F. A., Vorobyov, E. I., Pavlyuchenkov, Y. N., & Akimkin, V. V. 2020, *Astronomy Reports*, 64, 107
- Takahashi, S. Z. & Inutsuka, S.-i. 2014, *ApJ*, 794, 55
- Tanaka, K. E. I. & Omukai, K. 2014, *MNRAS*, 439, 1884
- Tominaga, R. T., Inutsuka, S.-i., & Kobayashi, H. 2021, *ApJ*, 923, 34
- Tominaga, R. T., Takahashi, S. Z., & Inutsuka, S.-i. 2019, *ApJ*, 881, 53
- Tsukamoto, Y., Machida, M. N., & Inutsuka, S.-i. 2021, *ApJ*, 920, L35
- Tsukamoto, Y., Takahashi, S. Z., Machida, M. N., & Inutsuka, S. 2015, *MNRAS*, 446, 1175
- Visser, R. G. & Ormel, C. W. 2016, *A&A*, 586, A66
- Vorobyov, E., Kulikov, I., Elbakyan, V., McKeivitt, J., & Guedel, M. 2024, *arXiv e-prints*, arXiv:2401.02205
- Vorobyov, E. I. 2013, *A&A*, 552, A129
- Vorobyov, E. I. 2016, *A&A*, 590, A115
- Vorobyov, E. I., Akimkin, V., Stoyanovskaya, O., Pavlyuchenkov, Y., & Liu, H. B. 2018, *A&A*, 614, A98
- Vorobyov, E. I. & Elbakyan, V. G. 2018, *A&A*, 618, A7
- Vorobyov, E. I. & Elbakyan, V. G. 2019, *A&A*, 631, A1
- Vorobyov, E. I., Elbakyan, V. G., Johansen, A., et al. 2023, *A&A*, 670, A81
- Vorobyov, E. I., Elbakyan, V. G., Omukai, K., et al. 2020a, *A&A*, 641, A72
- Vorobyov, E. I., Elbakyan, V. G., Takami, M., & Liu, H. B. 2020b, *A&A*, 643, A13
- Vorobyov, E. I., Matsukoba, R., Omukai, K., & Guedel, M. 2020c, *A&A*, 638, A102
- Vorobyov, E. I., Skliarevskii, A. M., Molyarova, T., et al. 2022, *A&A*, 658, A191
- Wang, J. & Fischer, D. A. 2015, *AJ*, 149, 14
- Ward, W. R. 1976, in *Frontiers of Astrophysics*, ed. E. H. Avrett, 1–40
- Weidenschilling, S. J. 1977, *MNRAS*, 180, 57
- Weidenschilling, S. J. 1980, *Icarus*, 44, 172
- Whipple, F. L. 1972, in *From Plasma to Planet*, ed. A. Elvius, 211
- Wong, Y. H. V., Hirashita, H., & Li, Z.-Y. 2016, *PASJ*, 68, 67
- Yang, C.-C., Johansen, A., & Carrera, D. 2017, *A&A*, 606, A80
- Yasui, C., Kobayashi, N., Saito, M., & Izumi, N. 2016, *AJ*, 151, 115
- Yasui, C., Kobayashi, N., Saito, M., Izumi, N., & Skidmore, W. 2021, *AJ*, 161, 139
- Yasui, C., Kobayashi, N., Tokunaga, A. T., Saito, M., & Tokoku, C. 2010, *ApJ*, 723, L113
- Yorke, H. W. & Bodenheimer, P. 2008, in *Astronomical Society of the Pacific Conference Series*, Vol. 387, *Massive Star Formation: Observations Confront Theory*, ed. H. Beuther, H. Linz, & T. Henning, 189
- Youdin, A. & Johansen, A. 2007, *ApJ*, 662, 613
- Youdin, A. N. & Goodman, J. 2005, *ApJ*, 620, 459
- Zhu, Z., Hartmann, L., Nelson, R. P., & Gammie, C. F. 2012, *ApJ*, 746, 110